

# Possible Evidence of Thermodynamic Equilibrium in Dark Matter Haloes

Joshua Davidson\*, Sanjoy K. Sarker† and Allen Stern‡

Department of Physics, University of Alabama,  
Tuscaloosa, Alabama 35487, USA

## ABSTRACT

After deducing the density profiles and gravitational potential functions of eight galaxies from the rotation velocity data from THINGS, we find that the density decreases exponentially with the potential in substantial regions of the haloes. Such behavior is in agreement with that of a single-component isothermal Boltzmann gas, and suggests that an effective description in terms of a Boltzmann gas is possible for dark matter in these regions. This could be an indication that dark matter self-interactions are sufficient in strength and number to lead to thermal equilibrium in these regions. We write down the dynamics and boundary conditions for a Boltzmann gas description and examine some of its qualitative and quantitative consequences. Solutions to the dynamical system are determined by three dimension-full parameters, and provide reasonable fits to the rotational velocity data in the regions where the Boltzmann-like behavior was found. Unlike in the usual approach to curve fitting, we do not assume a specific form for the dark matter density profile and we do not require a detailed knowledge of the baryonic content of the galaxy.

---

\*jadavidson@crimson.ua.edu

† ssarker@ua.edu

‡ astern@ua.edu

# 1 Introduction and Outline

The paradigm of collisionless cold dark matter has had much success in describing the large scale structure of the universe. Nevertheless, inconsistencies persist with observations at smaller scales. One example is the cusp singularity in the dark matter density profile, which is predicted by simulations of collisionless particles,[1] but is in contrast with observations, in particular, for dwarf galaxies.[2],[3] The possibility that such inconsistencies may be cured with the inclusion of non gravitational self-interactions was suggested a number of years ago.[4] The proposal of self-interacting dark matter (having interaction times less than the Hubble time) is not currently excluded, despite existing constraints on the interactions coming from halo shapes and cluster interactions. Numerous models for dark matter self-interactions have been considered, and their role in curing observational anomalies has been explored.[5],[6],[7],[8],[9],[10],[11],[12],[13] Since self-interactions among dark matter particles are not excluded, it is then reasonable to ask whether conditions may be suitable in galaxies for a gas of dark matter particles to reach a state of thermodynamic equilibrium. From the theoretical side, it is a non trivial problem to know precisely what conditions should be satisfied for this to occur since the nature of the interaction is unknown. However, it is possible to search for indications of thermal equilibrium in regions of galactic haloes from direct observations. This can be done using the rotation curve data, which is a central theme of the article.

Our paper contains two parts. In the first part (section 2), we search for regions in galactic halos that show behavior analogous to what one would expect from a classical (Boltzmann) gas in thermal equilibrium. In addressing this issue, we only need to require that the region of interest in the halo is approximately spherically symmetric and that the source of the rotation curves are circular orbits. Both of these assumptions are commonly utilized in curve fittings of the rotation velocity data. With these two assumptions one can simultaneously determine the halo density  $\rho$  and gravitational potential  $\phi$  from orbital speeds of HI gas in the halo. The assumption of spherical symmetry means that these quantities are functions of a single parameter. Rather than taking the parameter to be the radial coordinate  $r$ , we can write  $\rho$  as a function of  $\phi$ . (This is a single-valued function because  $\phi$  monotonically increases with  $r$ .) It is then of interest to search for some universal behavior for  $\rho(\phi)$ . In particular, an exponentially decreasing function would indicate agreement with a self-interacting classical gas in thermodynamic equilibrium. To be more specific, the determination of  $\phi(r)$  and  $\rho(r)$  from the circular orbital speed  $v(r)$  follows from simple classical physics considerations. The former is obtained by integrating Newton's law,

$$\frac{d\phi}{dr} = \frac{v^2(r)}{r}, \quad (1)$$

while the latter comes from the Poisson equation,  $\nabla^2\phi = 4\pi G\rho(r)$ ,  $G$  being the gravitational constant. Upon assuming spherical symmetry and then substituting (1) one gets

$$\rho(r) = \frac{1}{4\pi Gr^2} \frac{d}{dr} \left( rv^2(r) \right). \quad (2)$$

From  $\phi(r)$  and  $\rho(r)$ , we then obtain  $\rho(\phi)$ .

Before discussing analysis of the rotation curve data, it is useful to make a few remarks about the ideal case of *exactly* flat rotation curves, i.e.,  $v(r) = \text{constant}$ .  $\phi$  varies logarithmically in  $r$  in this case, while from (2) one gets that  $\rho(r) \propto 1/r^2$ . It is a well known curiosity that the combination of these two results gives an exponential behavior for  $\rho(\phi)$ , i.e.,  $\rho(\phi) \propto e^{-\phi/\phi_0}$ , where  $\phi_0$  is a constant associated with the so-called velocity dispersion. Therefore, the source of the gravitational potential responsible for

exactly flat rotation curves behaves in an identical manner to a single component isothermal Boltzmann gas.

Of course, a galactic system is not a single component system, and the density and gravitational potential get contributions from both dark matter and baryonic matter. Moreover, the above scenario is an oversimplification, since in nature, rotation curves are not exactly flat. On the other hand, the absence of exactly flat rotation curves from galaxies, does not rule out an exponential behavior for  $\rho(\phi)$ . For that reason it is of interest to make a more accurate determination of  $\rho(\phi)$  from the rotation curves in galactic haloes. We do so using the data from THINGS[14]. A local maximum can be identified for most of the rotation curves. So for them, there is always a small neighborhood where  $v$  is approximately constant, and it would come as no surprise to find that  $\rho$  decreases exponentially with  $\phi$  in that neighborhood. A more significant result would be to find exponential behavior for  $\rho(\phi)$  in a region that extends far beyond a local maximum. We present evidence that this is the case for eight galaxies (out of 19) in the THINGS survey. They are NGC 2841, NGC 5055, NGC 7331, NGC 2403, NGC 2903, NGC 3521, NGC 3198 and DD0 154. The results suggest that an effective Boltzmann gas description of dark matter is possible for certain regions of galactic haloes, more precisely, spherical shells  $R_G \leq r \leq R_{\max}$ . The constant  $1/\phi_0$  can be approximately determined for these regions, which can then be identified with the ratio of particle mass  $m$  with some effective temperature  $T$  (times Boltzmann's constant  $k_B$ ). In section 2 we estimate  $m/T$  for the eight galaxies in the relevant regions.

In the second part of the paper, beginning with section 3, we make a model utilizing the effective Boltzmann description. The dynamics of the model is taken to be that of a single-component self-gravitating isothermal gas, which is assumed to be valid for the spherical shell,  $R_G \leq r \leq R_{\max}$ . Along with spherical symmetry, the model makes the simplifying assumption that only dark matter is present at distances larger than  $R_G$ , and that all baryonic matter is contained within a sphere of radius  $R_G$ . (Dark matter is also assumed to be present in the region  $r < R_G$ .) The baryonic component nevertheless strongly influences the region of interest  $R_G \leq r \leq R_{\max}$ , as it contributes to the gravitational acceleration  $\frac{d\phi}{dr}$ , and thus is responsible for a tidal force on the isothermal gas. The pressure balance implicitly holds everywhere within and beyond the isothermal region, with the pressure within the isothermal region given by the ideal gas equation.

The relevant dynamical equation for such a system has been known for a long time.[15] It is the Emden equation, which is just the Poisson equation with an isothermal Boltzmann gas source. It has a well known solution, found by Emden, which satisfies the condition that it be nonsingular for *all* values of the radial coordinate,  $0 \leq r < \infty$ . The solution results from the boundary condition that states that the gravitational force vanishes at the origin. Emden's solution gives a unique density profile, and yields a flat rotation curve in the asymptotic limit  $r \rightarrow \infty$ .

Since for us the relevant domain is a spherical shell, the condition that the solution be nonsingular for all  $r$  is too restrictive, and we must seek alternative boundary conditions, and hence alternative solutions. The appropriate conditions for our case should be imposed at the inner boundary,  $r = R_G$ . The derivative of  $\phi$  at this point gives the gravitational attraction to the matter in the interior region  $r < R_G$ . The baryonic component dominates the interior region, and so it is largely responsible for the boundary conditions at  $r = R_G$ , and it contributes to the gravitational potential of the Boltzmann gas. In section 3, we show that a family of spherically symmetric solutions to the Emden equations results from such boundary conditions. They then lead to a family of density profiles that are parameterized by two dimensionless constants, which we denote by  $\kappa$  and  $\tau$ . The parameters can be expressed as functions of the total mass  $M_G$  in the interior region  $r < R_G$ , as well as  $R_G$  and the effective temperature

of the gas. The family of solutions contains Emden’s solution as a special case. Another special solution is one which gives an exactly flat rotation curve for all of  $R_G \leq r \leq R_{\max}$ .<sup>§</sup> It results from particular values of the two dimensionless parameters  $\kappa$  and  $\tau$ . Since the solution yields an exactly flat rotation curve it should serve as a crude fit to observations. From the crude fit one can determine the ratio  $m/T$  in terms of the orbital speed in the halo. For instance, from typical orbital speeds of  $\sim 200$  km/s, one gets  $m/T \sim 400$  eV per Kelvin. If one takes the analogy with the Boltzmann gas further and regards  $T$  as the temperature of a gas in equilibrium, the equipartition theorem for this system implies that the mean speed of the dark matter particles in the gas is of the same order of magnitude as the rotational speed for HI in the halo. So if the orbital speed is a few hundred km/s, the speed of the particles in the gas is also a few hundred km/s, and this result is independent of the dark matter mass. The details of this argument are given in Section 3.

We go beyond the crude approximation in section 4. There we perform fits of the rotation curve data to the solutions of the self-gravitating isothermal gas for the eight galaxies examined in section 2. The fits are applied only to the regions  $R_G \leq r \leq R_{\max}$  of the haloes where  $\rho(\phi)$  exhibited exponential behavior. Our approach is quite different from the usual approach to curve fitting, such as Navarro-Frenk-White (NFW) fits.[1] We do not assume any specific form for the dark matter density profile. Rather, the density  $\rho(r)$  is inferred from the fitted solution. We also do not require any detailed knowledge of the baryonic content of the galaxy. These details are often difficult to accurately determine, yet they play a crucial role in the usual approach to curve fitting. Moreover, results differ significantly from one mass model to another. In the usual approach to curve fitting, the matter contributions from the disk, bulge and HI gas must be subtracted from the rotation curve data. Here, on the other hand, it would be a mistake to subtract off the baryonic contribution to rotation velocity before doing the curve fitting. This is because the contribution of baryonic matter from the inner region  $r \leq R_G$  is already included in the gravitational potential  $\phi(r)$ . Moreover, the Boltzmann equation determines the actual rotational velocity, not individual contributions from the different components. Finally, while fits to rotational curve data are usually performed for the entire galaxy, here it makes sense to perform the fits to the Boltzmann gas only for the spherical shell,  $R_G \leq r \leq R_{\max}$ , where evidence for such a behavior has been found from the data.

While only two dimensionless parameters are needed to specify solutions to the Boltzmann equation, three *dimensionfull* parameters are required to fit the rotational velocity data. They are  $m/T$ , the density  $\rho(R_G)$  at  $r = R_G$  and the total mass  $M(R_G)$  contained inside the sphere of radius  $R_G$ . Not too surprisingly, the result for  $m/T$  obtained from the fit are reasonably consistent with the corresponding values obtained in section 2. We use the fit to estimate the mass  $M_{(R_G, R_{\max})}$  of the region  $R_G \leq r \leq R_{\max}$  exhibiting the Boltzmann behavior. In most cases, we find that this mass is larger than that of the inner region  $r \leq R_G$ . We also find that in most cases,  $M_{(R_G, R_{\max})}$  is larger than previous estimates of the total baryonic mass of the galaxy, obtained from mass models.[14] This lends support to the conclusion that the region  $R_G \leq r \leq R_{\max}$  exhibiting Boltzmann-like behavior contains a significant fraction of the total mass of the galaxy, and that it consists primarily of dark matter.

A summary of the results for the eight galaxies, including two tables, is given in section 5, along with concluding remarks.

---

<sup>§</sup> This solution has often been referred to as the ‘singular’ isothermal sphere because it is singular in the limit  $r = 0$ . For us, however, the solution is *nonsingular* because the origin is excluded from the domain.

## 2 Determination of $\rho(\phi)$ from rotation curve data

As stated in the introduction, the density function  $\rho(r)$  and gravitational potential  $\phi(r)$  in the halo can be numerically determined from the rotation velocity data under certain simplifying assumptions. The assumptions are that the system is spherically symmetric and that the rotation velocity data are attributed to circular orbits.  $\phi(r)$  and  $\rho(r)$  are obtained from  $v(r)$  using (1) and (2), respectively. The two functions can then be combined to determine  $\rho(\phi)$ . In order to search for Boltzmann-like behavior, it is useful to plot  $\log \rho$  versus  $\phi$ . We do this for the eight mentioned galaxies in the THINGS survey. Boltzmann-like behavior would correspond to a straight line with negative slope in the plot of  $\log \rho$  versus  $\phi$ , the slope being  $\phi_0$  or  $T/m$ . We also plot  $-\frac{d}{d\phi} \log \rho$  versus  $r$  for the eight galaxies. Boltzmann-like behavior would yield a constant in the latter graph, corresponding to the value of  $m/T$  for the gas.

The first step in the analysis is to fit the rotation velocity data to a smooth curve  $v(r)$ . We should mention that the results for  $\rho(\phi)$  are somewhat sensitive to how closely one fits the data to a smooth curve. In order to reduce the subjectivity of the analysis, we fit all eight galaxies in the sample to the same eight-parameter series, i.e.,  $\sum_{n=-3}^4 a_n r^n$ . Our analysis reveals an exponential behavior for regions of the haloes. This behavior becomes less evident if we make a cruder fit to the data, using only a few parameters. On the other side, additional features of the halo obscure the exponential behavior if one includes too many parameters.

The eight galaxies are organized into four categories: unbarred galaxies (NGC 2841, NGC 5055 and NGC 7331), weakly barred galaxies (NGC 2403, NGC 2903 and NGC 3521), a barred spiral galaxy (NGC 3198), and finally, a dwarf galaxy (DD0 154).

We begin with the unbarred galaxies. After first listing some relevant information for these galaxies, we then determine  $\log \rho(\phi)$  from the data.

### 2.1 NGC 2841

The morphology classification of NGC 2841 is SA(r)b. It is a flocculent, unbarred giant spiral galaxy, with a classical bulge and a significant population of blue stars. A certain mass model gives the disk and bulge masses for NGC 2841 of  $1.096 \times 10^{11} M_\odot$  and  $2.51 \times 10^{10} M_\odot$ , respectively.<sup>¶</sup> Using [16] the distance scale of the disk is  $\sim 3.5$  kpc. The HI gas mass for NGC 2841 is  $8.6 \times 10^9 M_\odot$ . [17] This is approximately 6% of the disk plus bulge mass, and so one would expect it to make only a small contribution to the total density in the halo. More background information about NGC 2841 can be found in [14].

The THINGS rotation velocity data for NGC 2841 is available at distances up to 51.6 kpc, or almost 15 times the distance scale of the disk. Figure 1 shows an eight-parameter fit of the rotation velocity data to the series  $\sum_{n=-3}^4 a_n r^n$  from  $r = 3.8$  to 51.6 kpc. The fit is done to the midpoints [corresponding to the dots] of the error bars. From the fitted function for  $v(r)$ , we obtain the gravitational potential  $\phi(r)$  by numerically integrating (1). The result is shown in figure 2. The density profile  $\rho(r)$  is found

<sup>¶</sup>More specifically, these values were obtained using models with fixed values of the mass to luminosity ratio and the diet Salpeter stellar initial mass function. (They were obtained from Table 3 of [14].) As we indicated previously, the baryonic masses for any given galaxy differ significantly from one model to another. These details play no direct role in the analyses we do here.

using (2), and is shown in figure 3.<sup>||</sup> The latter two plots are combined in figure 4 to give  $\log(\rho(r)/\rho_0)$  versus  $\phi(r)$ , where  $\rho_0$  is a constant with units of density. In the region  $7 < r < 22$  kpc, it approximately coincides with a straight line with negative slope. From this figure it thus appears that  $\rho(\phi)$  has an exponential behavior in the region  $7 < r < 22$  kpc, or approximately from 2 to 6 times the distance scale of the disk. Finally, in figure 5 we plot minus the derivative of  $\log \rho$  with  $\phi$  versus  $r$ . An approximately constant value of  $\sim 190$  eV/Kel is obtained for  $-\frac{d \log \rho}{d \phi}$  over the range  $7 < r < 22$  kpc, which is shown in the inset. Therefore this region is consistent with the description of a Boltzmann gas with  $m/T \sim 190$  eV/Kel.  $-\frac{d \log \rho}{d \phi}$  gradually increases to  $\sim 250$  eV/Kel over the range  $20 < r < 30$  kpc, before rapidly decreasing beyond 30 kpc.

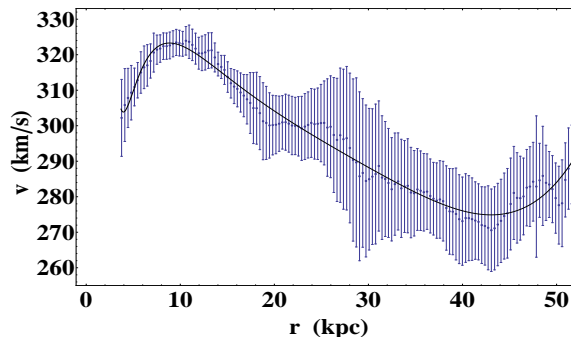


Figure 1: Eight-parameter series fit of rotation velocity data for NGC 2841 from  $r = 3.8$  to 51.6 kpc.

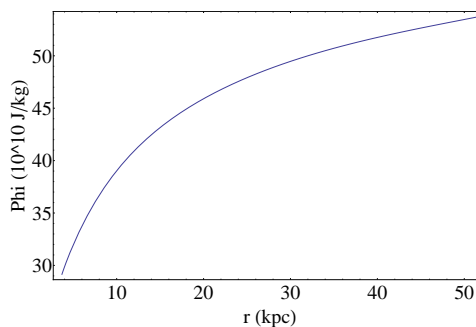


Figure 2: Resulting gravitational potential versus  $r$  for NGC 2841 from  $r = 3.8$  to 51.6 kpc. The zero of the potential is at  $r = 3.8$ .

---

<sup>||</sup>Figure 3 exhibits a region beyond 40 kpc where the density increases with increasing  $r$ . Similar results are seen for very distant regions of NGC 7331, NGC 2903, NGC 3521 and NGC 3198. This behavior is presumably unphysical, and so if one can trust the fits in these regions, it may indicate that the two assumptions (spherical symmetry and circular orbits) used in obtaining  $\rho(r)$  are invalid for these particular regions. In any case, these regions are far beyond the domains of interest of our paper.

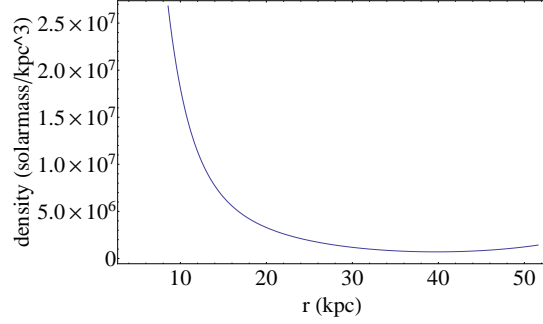


Figure 3: Resulting density versus  $r$  for NGC 2841 from  $r = 3.8$  to  $51.6$  kpc.

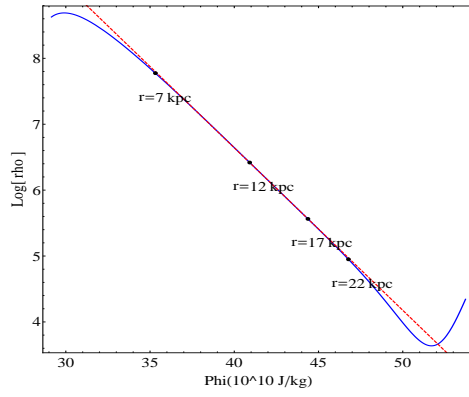


Figure 4:  $\log(\text{density}/\text{constant})$  versus the gravitational potential for NGC 2841 for  $r = 3.8$  to  $51.6$  kpc. It is compared to a straight line (red, dashed) with slope  $\approx -190$  eV/Kel. The two plots approximately coincide for  $7 < r < 22$  kpc.

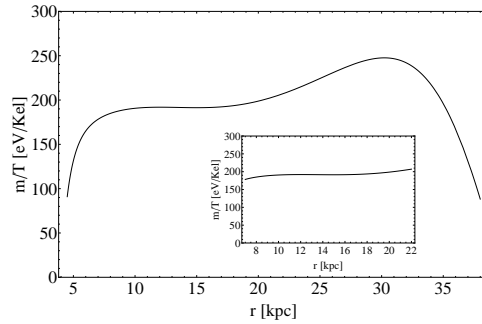


Figure 5:  $-\frac{d \log \rho}{d \phi}$  versus  $r$  for NGC 2841. The plot is approximately constant for the domain  $7 < r < 22$  kpc, which is shown in the inset.

## 2.2 NGC 5055

The morphology classification of NGC 5055 is SA(rs)bc. It is an unbarred spiral galaxy, with an extended warp at end of the optical disk. It has a regular structure with well defined flocculent spiral arms, and is part of the M51 group of galaxies. Mass models ([see [14]) give the disk and bulge masses for NGC 5055 of  $1.203 \times 10^{11} M_{\odot}$  and  $2.09 \times 10^9 M_{\odot}$ . The distance scale of the disk is  $\sim 3.622$  kpc. [16] The HI gas mass for NGC 5055 is  $.91 \times 10^{10} M_{\odot}$ , [17] which is approximately 7% of the disk plus bulge mass.

THINGS rotation velocity data are available at distances up to  $\sim 44.4$  kpc, around 12 times the distance scale of the disk. An eight-parameter series fit, again using  $\sum_{n=-3}^4 a_n r^n$ , of the data from  $r = .2$  to 44.4 kpc appears in figure 6. Here we don't include a plot of  $\phi(r)$  and  $\rho(r)$ , but give the plot of  $\log(\rho(r)/\text{constant})$  versus  $\phi(r)$  in figure 7. An approximate straight line with negative slope is recovered upon restricting the radial coordinate to  $10 < r < 25$  kpc. In figure 8 we plot minus the derivative of  $\log \rho$  with  $\phi$  versus  $r$ . It is approximately constant in the domain  $10 < r < 25$  kpc (shown in the inset), with an average value of  $\sim 440$  eV/Kel.  $-\frac{d \log \rho}{d \phi}$  reaches a minimum value of  $\sim 375$  eV/Kel at  $r \approx 4$  kpc, before rapidly increasing at smaller distances.

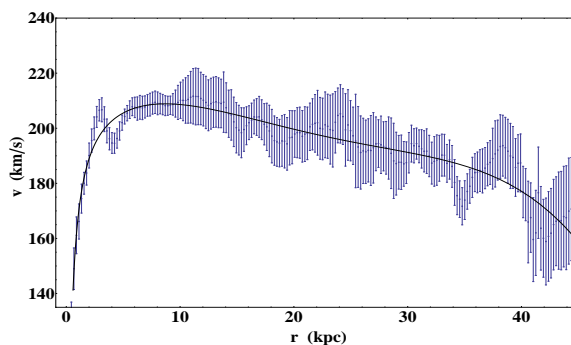


Figure 6: Series fit of rotation velocity data for NGC 5055 from  $r = .2$  to 44.4 kpc.

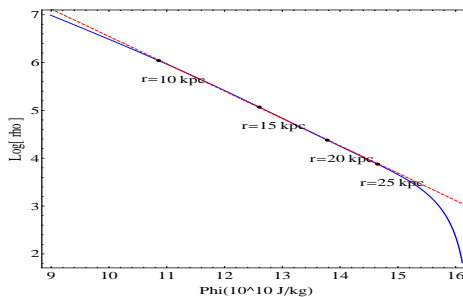


Figure 7:  $\log(\text{density}/\text{constant})$  versus the gravitational potential for NGC 5055 for  $r = 6.5$  to 37.5 kpc. It is compared to a straight line (red, dashed) with slope  $\approx -440$  eV/Kel. The two plots approximately coincide for  $10 < r < 25$  kpc.



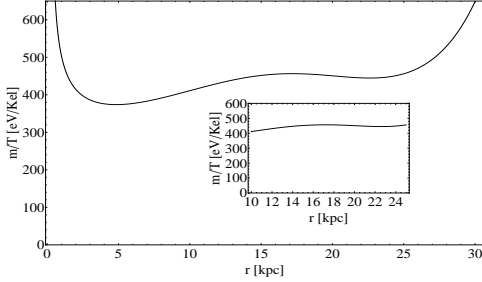


Figure 8:  $-\frac{d \log \rho}{d \phi}$  versus  $r$  for NGC 5055. The plot is approximately constant for the domain  $10 < r < 25$  kpc, which is shown in the inset.

### 2.3 NGC 7331

The morphology classification of NGC 7331 is SA(s)b. It is regular at large scales, but spiral arms cause wiggles in velocity contours, and there are large differences in the rotation curve for the approaching and receding sides.[14] Mass models give the disk and bulge masses for NGC 7331 of  $1.66 \times 10^{11} M_{\odot}$  and  $1.74 \times 10^{10} M_{\odot}$ . The distance scale of the disk is  $\sim 3.2$  kpc. [16] The HI gas mass for NGC 7331 is  $.91 \times 10^{10} M_{\odot}$ , [17] which is approximately 5% of the disk plus bulge mass.

THINGS rotation velocity data are available at distances up to  $\sim 24.4$  kpc, or over seven times the distance scale of the disk. The eight-parameter series fit of rotation velocity data from  $r = 3.3$  to 24.4 kpc appears in figure 9. The resulting plot of  $\log(\rho(r)/\text{constant})$  versus  $\phi(r)$  is given in figure 10. An approximate straight line with negative slope is recovered upon restricting the radial coordinate to  $8 < r < 16$  kpc. In figure 11 we plot minus the derivative of  $\log \rho$  with  $\phi$  versus  $r$ . It is approximately constant in the domain  $8 < r < 16$  kpc (shown in the inset), with an average value of  $\sim 260$  eV/Kel.  $-\frac{d \log \rho}{d \phi}$  reaches a maximum value of  $\sim 340$  eV/Kel at  $r \approx 5.5$  kpc.

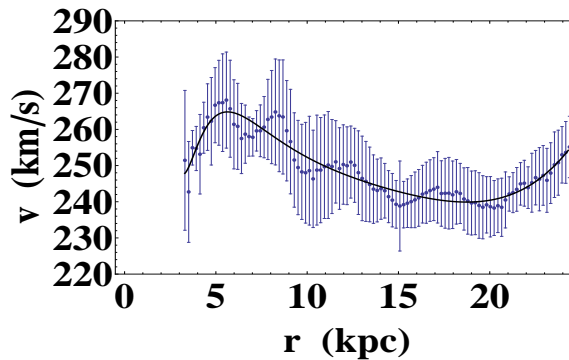


Figure 9: Series fit of rotation velocity data for NGC 7331 from  $r = 3.3$  to 24.4 kpc.

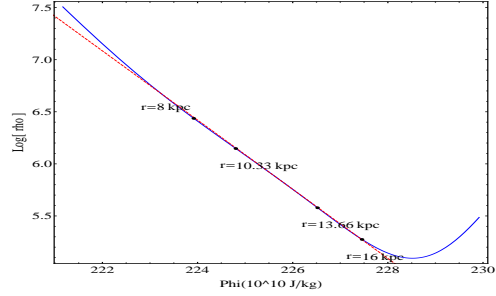


Figure 10:  $\log(\text{density}/\text{constant})$  versus the gravitational potential for NGC 7331 for  $r = 6$  to 24.3 kpc. It is compared to a straight line (red, dashed) with slope  $\approx -260$  eV/Kel. The two plots approximately coincide for  $8 < r < 16$  kpc.

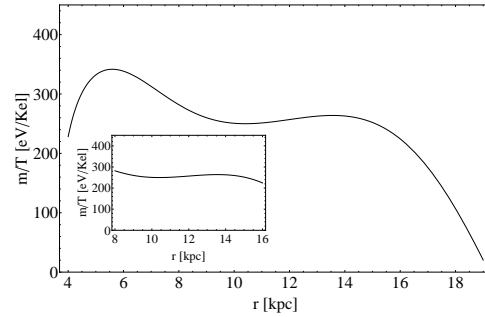


Figure 11:  $-\frac{d \log \rho}{d \phi}$  versus  $r$  for NGC 7331. The plot is approximately constant over the domain  $8 < r < 16$  kpc, which is shown in the inset.

We next repeat the previous analysis for weakly barred spiral galaxies: NGC 2403, NGC 2903 and NGC 3521.

## 2.4 NGC 2403

The morphology classification of NGC 2403 is SAB(s)cd. Mass models (see [14]) give the disk and bulge masses for NGC 2403 of  $4.68 \times 10^9 M_\odot$  and  $4.27 \times 10^8 M_\odot$ , respectively. The distance scale of the disk is  $\sim 2.7$  kpc. [16] The HI gas mass for NGC 2403 is  $2.58 \times 10^9 M_\odot$ , [17] which is approximately 50% of the disk plus bulge mass.

THINGS rotation velocity data are available at distances up to  $\sim 24$  kpc, or almost nine times the distance scale of the disk. The eight-parameter series fit of rotation velocity data from  $r = .1$  to 24 kpc appears in figure 12. The resulting plot of  $\log(\rho(r)/\text{constant})$  versus  $\phi(r)$  is given in figure 13. An approximate straight line with negative slope is recovered upon restricting the radial coordinate to  $3 < r < 10$  kpc. In figure 14 we plot minus the derivative of  $\log \rho$  with  $\phi$  versus  $r$ . It is approximately constant in the domain  $3 < r < 10$  kpc (shown in the inset), with an average value of  $\sim 1100$  eV/Kel.

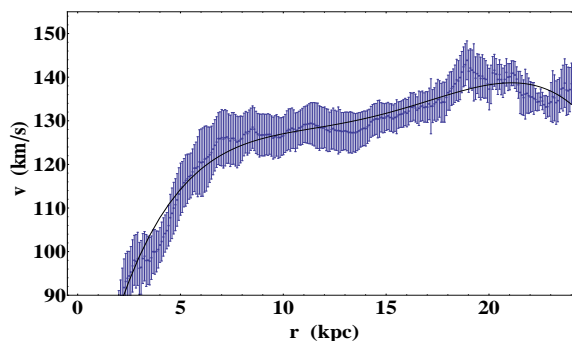


Figure 12: Eight-parameter series fit of rotation velocity data for NGC 2403 from  $r = .1$  to 24 kpc.

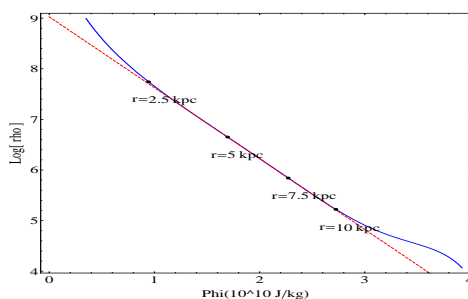


Figure 13:  $\log(\text{density}/\text{constant})$  versus the gravitational potential for NGC 2403 for  $r = 1$  to 20 kpc. It is compared to a straight line (red, dashed) with slope  $\approx -1100$  eV/Kel. The two plots approximately coincide for  $3 < r < 10$  kpc.

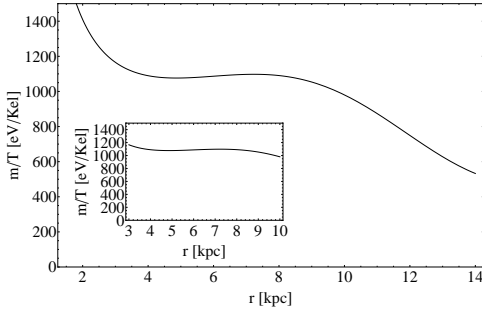


Figure 14:  $-\frac{d \log \rho}{d \phi}$  versus  $r$  for NGC 2403. The plot is approximately constant over the domain  $3 < r < 10$  kpc, which is shown in the inset.

## 2.5 NGC 2903

The morphology classification of NGC 2903 is SAB(rs)bc. It has tightly wound spiral arms. Mass models (see [14]) give the disk and bulge masses for NGC 2903 of  $1.41 \times 10^{10} M_{\odot}$  and  $2.14 \times 10^9 M_{\odot}$ , respectively. The distance scale of the disk is  $\sim 3.0$  kpc. [16] The HI gas mass for NGC 2903 is  $4.35 \times 10^9 M_{\odot}$ , [17] which is approximately 27% of the disk plus bulge mass.

THINGS rotation velocity data are available at distances up to 31 kpc, which is over ten times the distance scale of the disk. An eight-parameter series fit of rotation velocity data from  $r = .3$  to 31 kpc appears in figure 15. The resulting plot of  $\log(\rho(r)/\text{constant})$  versus  $\phi(r)$  is given in figure 16. An approximate straight line with negative slope is recovered upon restricting the radial coordinate to  $3 < r < 9$  kpc. In figure 17 we plot minus the derivative of  $\log \rho$  with  $\phi$  versus  $r$ . It is approximately constant in the domain  $3 < r < 9$  kpc (shown in the inset), with an average value of  $\sim 490$  eV/Kel. If one extends the domain up to 25 kpc, the value of  $m/T$  varies from  $\sim 350$  to  $\sim 650$  eV/Kel.

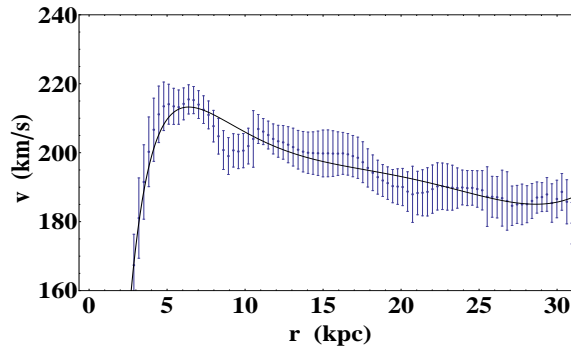


Figure 15: Series fit of rotation velocity data for NGC 2903 from  $r = .3$  to 31 kpc .

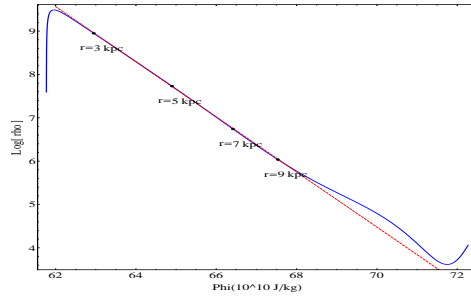


Figure 16:  $\log(\text{density}/\text{constant})$  versus the gravitational potential for NGC 2903 for  $r = 1$  to 31 kpc. It is compared to a straight line (red, dashed) with slope  $\approx -490$  eV/Kel. The two plots approximately coincide for  $3 < r < 9$  kpc.

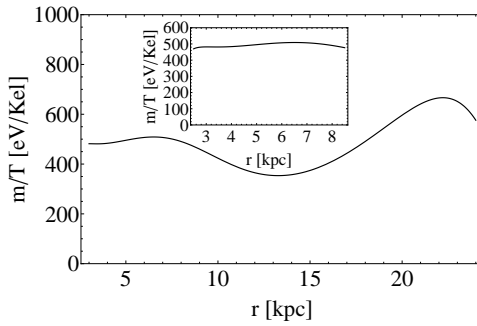


Figure 17:  $-\frac{d \log \rho}{d \phi}$  versus  $r$  for NGC 2903. The plot is approximately constant over the domain  $3 < r < 9$  kpc, which is shown in the inset.

## 2.6 NGC 3521

The morphology classification of NGC 3521 is SAB(rs)bc. It has a flocculent spiral structure and a negligible bulge. Mass models (see [14]) give the disk mass for NGC 3521 of  $1.23 \times 10^{11} M_{\odot}$ , with a corresponding distance scale of  $\sim 3.3$  kpc. [16] The HI gas mass for NGC 3521 is  $.802 \times 10^{10} M_{\odot}$ , [17] which is approximately 6.5% of the disk mass.

THINGS rotation velocity data are available at distances up to 35.5 kpc, which is over ten times the distance scale of the disk. An eight-parameter series fit of rotation velocity data from  $r = 3.2$  to 35.5 kpc appears in figure 18. The resulting plot of  $\log(\rho(r)/\text{constant})$  versus  $\phi(r)$  is given in figure 19. An approximate straight line with negative slope is recovered upon restricting the radial coordinate to  $7 < r < 15$  kpc. In figure 20 we plot minus the derivative of  $\log \rho$  with  $\phi$  versus  $r$ . It is approximately constant in the domain  $7 < r < 15$  kpc (shown in the inset), with an average value of  $\sim 380$  eV/Kel. A minimum of  $\sim 230$  eV/Kel occurs at  $\sim 4$  kpc.

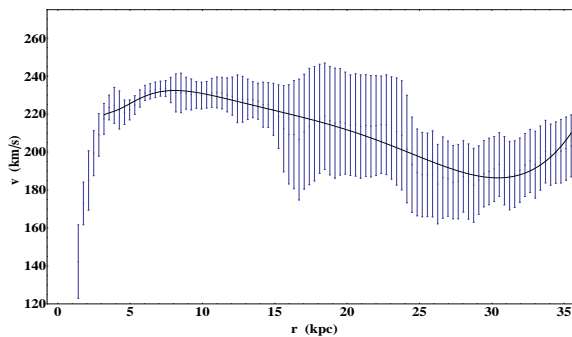


Figure 18: Series fit of rotation velocity data for NGC 3521 from  $r = 3.2$  to 35.5 kpc.

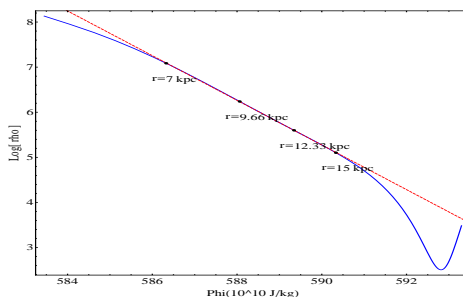


Figure 19:  $\log(\text{density}/\text{constant})$  versus the gravitational potential for NGC 3521 for  $r = 4$  to 30 kpc. It is compared to a straight line (red, dashed) with slope  $\approx -380$  eV/Kel . The two plots approximately coincide for  $7 < r < 15$  kpc.

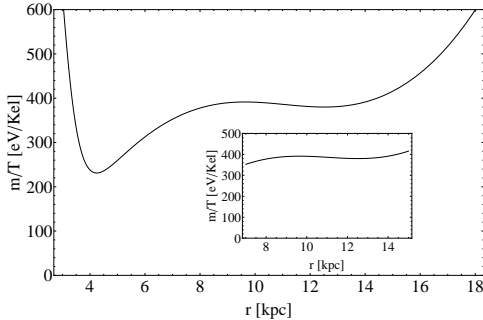


Figure 20:  $-\frac{d \log \rho}{d \phi}$  versus  $r$  for NGC 3521. The plot is approximately constant over the domain  $7 < r < 15$  kpc, which is shown in the inset.

We next consider the barred spiral galaxy NGC 3198.

## 2.7 NGC 3198

The morphology classification of NGC 3198 is SB(rs)c. This galaxy has two well-defined spiral arms, and has indications of a modest warp. Mass models (see [14]) give the disk and bulge masses for NGC 3198 of  $2.82 \times 10^{10} M_{\odot}$  and  $2.88 \times 10^9 M_{\odot}$ , respectively. The distance scale of the disk is  $\sim 4.0$  kpc. [16] The HI gas mass for NGC 3198 is  $1.017 \times 10^{10} M_{\odot}$ , [17] which is approximately 33% of the disk plus bulge mass.

THINGS rotation velocity data are available at distances up to 38.5 kpc, which is over nine times the distance scale of the disk. The eight-parameter series fit of rotation velocity data from  $r = 4.1$  to 38.5 kpc appears in figure 21. The resulting plot of  $\log(\rho(r)/\text{constant})$  versus  $\phi(r)$  is given in figure 22. An approximate straight line with negative slope is recovered upon restricting the radial coordinate to  $5 < r < 15$  kpc. In figure 23 we plot minus the derivative of  $\log \rho$  with  $\phi$  versus  $r$ . It ranges between  $\sim 750$  eV/Kel and  $\sim 950$  eV/Kel and has an average value of  $\sim 820$  eV/Kel for the domain  $5 < r < 25$  kpc.

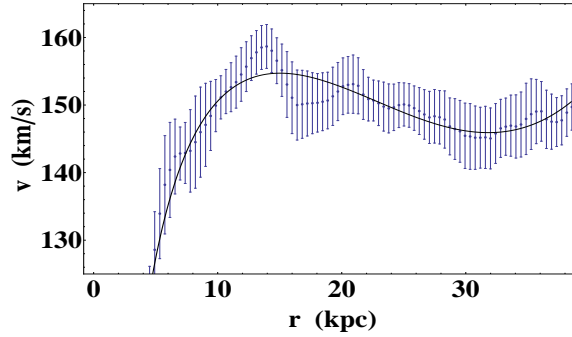


Figure 21: Eight-parameter series fit of rotation velocity data for NGC 3198 from  $r = 4.1$  to 38.5 kpc.

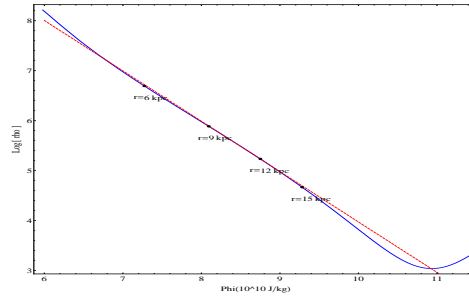


Figure 22:  $\log(\text{density}/\text{constant})$  versus the gravitational potential for NGC 3198 for  $r = 2$  to 39.5 kpc. It is compared to a straight line (red, dashed) with slope  $\approx -820$  eV/Kel. The two plots approximately coincide for  $5 < r < 15$  kpc.

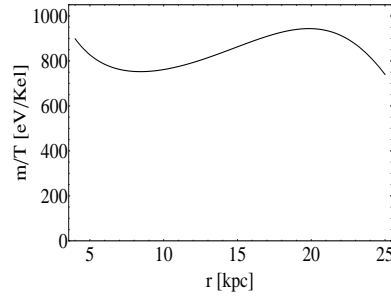


Figure 23:  $-\frac{d \log \rho}{d \phi}$  versus  $r$  for NGC 3198. The plot ranges between  $\sim 750$  eV/Kel and  $\sim 950$  eV/Kel for the domain  $5 < r < 25$  kpc.



Finally, we repeat the analysis for the dwarf galaxy DD0 154.

## 2.8 DD0 154

The morphology classification of DD0 154 is IB(s)m. It is a gas-rich dwarf irregular galaxy with a negligible bulge. Mass models (see [14]) give the disk mass for DD0 154 of  $2.63 \times 10^7 M_{\odot}$ , with a corresponding distance scale of  $\sim .8$  kpc. [16] The HI gas mass for DD0 154 is  $3.58 \times 10^8 M_{\odot}$ , [17] which is approximately 13.6 times the disk mass.

THINGS rotation velocity data are available at distances up to 8 kpc, or ten times the distance scale of the disk. The eight-parameter series fit of rotation velocity data from  $r = .3$  to 8 kpc appears in figure 24. The resulting plot of  $\log(\rho(r)/\text{constant})$  versus  $\phi(r)$  is given in figure 25. An approximate straight line with negative slope is recovered upon restricting the radial coordinate to  $1.5 < r < 4.5$  kpc. In figure 26 we plot minus the derivative of  $\log \rho$  with  $\phi$  versus  $r$ . It ranges between  $\sim 7500$  eV/Kel and  $\sim 10000$  eV/Kel and has an average value of  $\sim 8600$  eV/Kel for the domain  $1.5 < r < 6.5$  kpc.

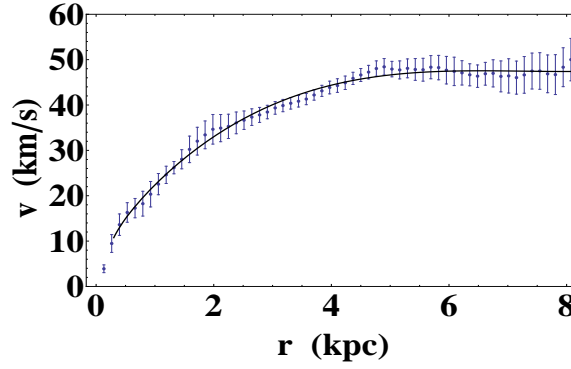


Figure 24: Eight-parameter series fit of rotation velocity data for DD0 154 from  $r = .3$  to 8 kpc.

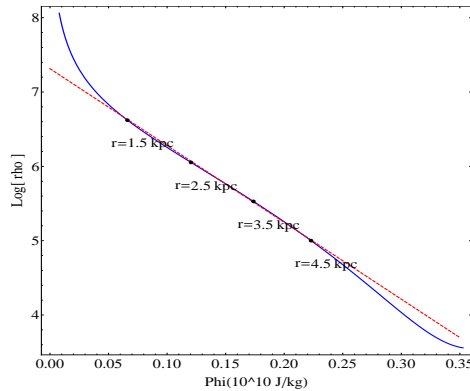


Figure 25:  $\log(\text{density}/\text{constant})$  versus the gravitational potential for DD0 154 for  $r = .3$  to 8 kpc. It is compared to a straight line (red, dashed) with slope  $\approx -8600$  eV/Kel. The two plots approximately coincide for  $1.5 < r < 4.5$  kpc.

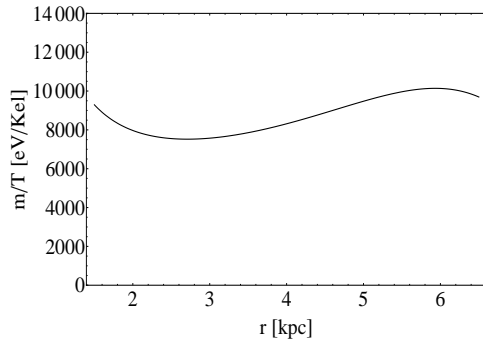


Figure 26:  $-\frac{d \log \rho}{d \phi}$  versus  $r$  for DD0 154. The plot ranges between  $\sim 7500$  eV/Kel and  $\sim 10000$  eV/Kel over the domain  $1.5 < r < 6.5$  kpc.

### 3 An effective theory

In the previous section we have presented evidence of Boltzmann-like behavior in regions of haloes of eight galaxies in the THINGS survey. Here we model the Boltzmann behavior by writing down the dynamics for a self-gravitating gas in thermodynamic equilibrium in an external gravitational field. The relevant domain for the model is a finite shell, associated with the regions where the exponential behavior was found for  $\rho$  versus  $\phi$ . Here we discuss the parameter space of the solutions of the model, along with consistency checks. Fits of the rotation curves to the solutions will be made in the following section.

#### 3.1 Dynamics and boundary conditions

Here we write down an effective thermodynamic model for regions, corresponding to spherical shells  $R_G \leq r \leq R_{\max}$ , where the Boltzmann gas is valid. More specifically, it is the description of a self-gravitating isothermal gas, subject to an external gravitational potential. The total gravitational potential is again denoted by  $\phi$ , which includes contributions from the gravitational self-interactions of the gas, as well as the external tidal force. We shall assume that the gas consists of only one type of particle, with mass  $m$ , and that  $\phi$  is slowly varying with respect to the average interparticle distance. As in the previous section, we assume that spherical symmetry holds, at least at lowest order, and so quantities of interest, such as  $\phi$  and the average density  $\rho$  are functions only of the radial variable. It is desirable to have the radius  $R_G$  of the inner boundary sufficiently larger than the distance scale of the disk. (This was generally the case for the examples considered in the previous section. For instance,  $R_G$  was approximately twice the disk scale for NGC 2841.) Then one expects that deviations from spherical symmetry and contributions from the baryonic matter to total density  $\rho$  in the spherical shell can be ignored at lowest order.

We first impose boundary conditions at  $r = R_G$ . The value of  $\phi$  at the boundary is arbitrary. It is convenient to choose it to be zero.\*\* Then for a Boltzmann gas one has

$$\rho(r) = \rho(R_G) e^{-m\phi(r)/k_B T} \quad (3)$$

---

\*\*Our fitting procedure will not depend on this choice. The fits determine values of  $\rho(R_G)$  and  $m/T$  in the density formula (3). The addition of a constant to the potential can be absorbed in  $\rho(R_G)$ .

On the other hand, the value of  $\frac{d\phi}{dr}$  at  $r = R_G$  must be identified with the acceleration of gravity at the inner boundary of the spherical shell. Thus

$$\phi(R_G) = 0 \quad \frac{d\phi}{dr} \Big|_{r=R_G} = \frac{GM_G}{R_G^2}, \quad (4)$$

$M_G$  is the total mass inside the sphere of radius  $R_G$ . The model is thus defined by the two boundary conditions and the Poisson equation

$$\frac{1}{r^2} \frac{d}{dr} \left( r^2 \frac{d\phi}{dr} \right) = 4\pi G \rho(R_G) e^{-m\phi(r)/k_B T}, \quad R_G \leq r \leq R_{\max} \quad (5)$$

The pressure balance implicitly holds everywhere within and beyond the isothermal region, including at the interfaces between the regions. The pressure within the isothermal region is given by the ideal gas equation  $P(r) = \rho(r)kT/m$ .

### 3.2 Solutions

To examine the space of solutions it is convenient to do a rescaling to the dimensionless variables  $x = \frac{r}{R_G}$  and  $\chi = \frac{R_G}{GM_G} \phi$ . (5) simplifies to

$$\frac{1}{x^2} \frac{d}{dx} \left( x^2 \frac{d\chi}{dx} \right) = 3\kappa e^{-\frac{\chi(x)}{\tau}}, \quad 1 \leq x \leq x_{\max}, \quad (6)$$

where  $x_{\max} = R_{\max}/R_G$ , and the boundary conditions become

$$\chi(1) = 0 \quad \frac{d\chi}{dx} \Big|_{x=1} = 1 \quad (7)$$

$\kappa$  and  $\tau$  are independent dimensionless parameters determining the solutions. They depend, among other things, on  $R_G$  and  $M_G$ .  $\kappa$  is the ratio of  $\rho(R_G)$  to the mean mass density in the interior of the sphere of radius  $R_G$ , i.e.,  $\rho_G = \frac{M_G}{\frac{4}{3}\pi R_G^3}$ , while  $\tau$  is a rescaled temperature

$$\kappa = \frac{\frac{4}{3}\pi R_G^3 \rho(R_G)}{M_G} \quad \tau = \frac{k_B T}{mv_{x=1}^2}, \quad (8)$$

where  $v_{x=1}$  is the speed of objects undergoing circular orbits at  $r = R_G$ . It is given by  $v_{x=1}^2 = GM_G/R_G$ . From solutions to (6) and (7) one can then determine the orbital speed  $v(x)$  at any value of the radial coordinate, along with the total mass  $M(x)$  enclosed in a sphere of radius  $x$ ,  $1 \leq x \leq x_{\max}$ . They are given respectively by

$$\left( \frac{v}{v_{x=1}} \right)^2 = x \frac{d\chi}{dx} \quad \text{and} \quad \frac{M(x)}{M_G} = 3\kappa \int_1^x dx' x'^2 e^{-\frac{\chi(x')}{\tau}} \quad (9)$$

Eq. (6) is the spherically symmetric Lane-Emden equation for infinite polytropic index, which is often referred to as the Emden equation.[15] Various techniques have been employed to obtain its solutions, and application to galactic dynamics has been discussed. (See for example, [18],[19],[20],[21]. Axially symmetric solutions with rotation have also been obtained.[22]) Boundary conditions for this equation are standardly imposed at the origin, where the gravitational force is required to vanish, i.e.,  $\frac{d\chi}{dx} \Big|_{x=0} = 0$ .<sup>††</sup> This boundary condition leads to a solution known as the isothermal sphere, which was first found by Emden.

---

<sup>††</sup> $\chi$  is often set to zero, as well, at the origin, but this is a gauge condition which can be removed with a redefinition of  $\kappa$ .

In our case, the Boltzmann gas description is not valid outside the domain  $1 \leq x \leq x_{\max}$ , and it is then appropriate to impose boundary conditions at  $x = 1$ , as we have done in (7). A two-parameter (i.e.,  $\kappa$  and  $\tau$ ) family of solutions to the Emden equations result from the boundary conditions (7).

The solutions contain Emden's isothermal sphere as a special case. That is, a subset of the solutions to (6) and (7) can be consistently continued from  $x = 1$  to the origin, where  $\left. \frac{d\chi}{dx} \right|_{x=0} = 0$ .  $\kappa$  and  $\tau$  are not independent for the subset. To see this one can do another rescaling of the field,  $\chi \rightarrow \tilde{\chi} = \chi/\tau$ , and the coordinate,  $x \rightarrow \tilde{x} = \sqrt{\frac{3\kappa}{\tau}} x$ , thereby removing the parameters from the differential equation (6), and putting them instead in the boundary conditions. Then

$$\frac{1}{\tilde{x}^2} \frac{d}{d\tilde{x}} \left( \tilde{x}^2 \frac{d\tilde{\chi}}{d\tilde{x}} \right) = e^{-\tilde{\chi}(\tilde{x})}, \quad (10)$$

with

$$\tilde{\chi} \Big|_{\tilde{x}=\sqrt{\frac{3\kappa}{\tau}}} = 0 \quad \frac{d\tilde{\chi}}{d\tilde{x}} \Big|_{\tilde{x}=\sqrt{\frac{3\kappa}{\tau}}} = \frac{1}{\sqrt{3\kappa\tau}} \quad (11)$$

For generic values of  $\kappa$  and  $\tau$ , the boundary conditions (11) cannot be generated by integrating the Emden equation from the origin, starting from  $\left. \frac{d\tilde{\chi}}{d\tilde{x}} \right|_{\tilde{x}=0} = 0$  and any  $\tilde{\chi}(0)$ . [ $\tilde{\chi}(0)$  must be negative since  $\tilde{\chi}$  grows with increasing  $\tilde{x}$ .] If one were to impose the boundary condition  $\left. \frac{d\tilde{\chi}}{d\tilde{x}} \right|_{\tilde{x}=0} = 0$ , along with some  $\tilde{\chi}(0) < 0$ , one can integrate the Emden equations to find the intersection of  $\tilde{\chi}(\tilde{x})$  with the  $\tilde{x}$ -axis, along with the slope of the function at that point. The result, along with (11), can then be used to numerically solve for specific values of  $\kappa$  and  $\tau$ , associated with the subset of isothermal spheres.

Another special solution to the Emden equation is the 'singular' isothermal sphere. It has the analytic expression

$$\chi(x) = \tau \log \left( \frac{3\kappa x^2}{2\tau} \right) \quad (12)$$

It is called singular because it is ill-defined at the origin (for any values of  $\kappa$  and  $\tau$ ). Rather than satisfying  $\left. \frac{d\chi}{dx} \right|_{x=0} = 0$ , the acceleration of gravity diverges at the origin. On the other hand, (12) is mathematically and physically well defined for the domain of interest here,  $1 \leq x \leq x_{\max}$ . It satisfies the boundary conditions (7) for particular values of  $\tau$  and  $\kappa$ , namely  $\tau = \frac{1}{2}$  and  $\kappa = \frac{1}{3}$ , or in terms of dimensionfull quantities,

$$\rho(R_G) = \frac{M_G}{4\pi R_G^3} \quad \frac{m}{T} = \frac{2k_B}{v_{x=1}^2} \quad (13)$$

From  $v_{x=1}^2 = GM_G/R_G$ , one finds that  $m/T$  in (13) is determined by the baryonic matter and dark matter contained in  $r < R_G$ . Using (9), one gets that the solution (12) has an exactly flat rotation curve,  $v = v_{x=1}$  for all  $x > 0$ , and a linearly increasing mass function  $M(x) = (x - 1) M_G$ . Since this behavior is roughly what is observed for all galactic haloes, (13) should provide crude estimates for  $\rho(R_G)$  and  $m/T$ . In section 4 we shall compare these estimates to values extracted from fits to the rotation curve data, and we can compare the fitted values of  $\kappa$  and  $\tau$  to this special case.

Although eq. (12) is not a solution for arbitrary values of  $\tau$  and  $\kappa$ , it does describe the behavior of generic solutions as  $x \rightarrow \infty$ .<sup>‡‡</sup> So in the asymptotic region of the solution (which may be beyond the relevant physical domain,  $1 \leq x \leq x_{\max}$ ), the orbital speed goes to a constant value, specifically

$$v_\infty = \sqrt{2\tau} v_{x=1} = \sqrt{\frac{2k_B T}{m}}, \quad (14)$$

<sup>‡‡</sup> To see this we can do another change of coordinates and rewrite the differential equation in terms of  $y = \log x$ . Upon assuming that  $\frac{d^2\chi}{dy^2} \ll \frac{d\chi}{dy}$  when  $y \rightarrow \infty$ , one gets  $\frac{d\chi}{dy} \sim 3\kappa \exp(2y - \chi(y)/\tau)$ , the solution of which is (12).

for any  $\kappa > 0$ . (Of course,  $v \rightarrow 0$  as  $x \rightarrow \infty$  in the absence of any matter source in the region, i.e.,  $\kappa = 0$ .) This is illustrated in figures 27 and 28. There we plot  $v/v_{x=1}$  for numerical solutions to (6) and (7) associated with various values of  $\tau$  and  $\kappa$  [including the values  $\tau = \frac{1}{2}$  and  $\kappa = \frac{1}{3}$  corresponding to the analytic solution (12)].

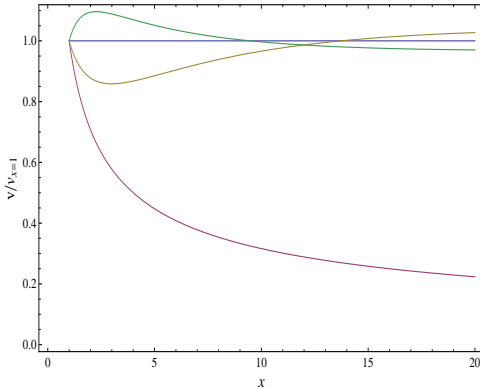


Figure 27:  $v/v_{x=1}$  is plotted versus  $x$  for  $\tau = \frac{1}{2}$  and  $\kappa = 0, \frac{1}{6}, \frac{1}{3}$  and  $\frac{1}{2}$ . The values of  $\kappa$  are listed in ascending order of the slope at  $x = 1$ , with  $\kappa = 0$  corresponding to no halo.

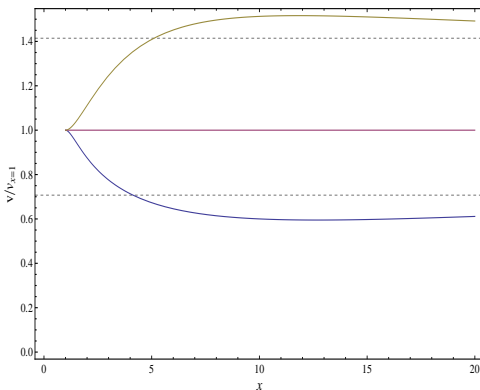


Figure 28:  $v/v_{x=1}$  is plotted versus  $x$  for  $\kappa = \frac{1}{3}$  and  $\tau = \frac{1}{4}, \frac{1}{2}$  and 1. The values of  $\tau$  are listed in ascending order of the slope at  $x = 1$ . The limiting value of  $v/v_{x=1}$  is  $\sqrt{2\tau}$ , which is indicated for the top and bottom curves by the dashed gridlines.

### 3.3 Consistency checks

Since we are dealing with an Boltzmann gas description, it is reasonable to regard the effective temperature as a measure of the average kinetic energy of the dark matter particles. Then a simple application of the equipartition theorem gives an rms speed of  $u = \sqrt{3k_B T/m}$ , assuming no internal structure for the particles. This is of the same order as the average orbital speed of the HI gas in the halo. From (14), one gets  $u = \sqrt{\frac{3}{2}}v_\infty$ , where  $v_\infty$  was the orbital speed in the limit  $r$  tends to infinity. Since orbital speeds in haloes are nonrelativistic, the particles in this Boltzmann gas description must also be nonrelativistic. This provides one consistency check of the model, as no relativistic corrections need to be considered.

Another consistency check comes from examining the number density  $n(r) = \rho(r)/m$ . A Boltz-

mann gas description necessitates that the particles behave classically. This means that the de Broglie wavelength  $\lambda$  is much less than the interparticle distance,

$$\lambda n^{1/3}(r) \ll 1 \quad (15)$$

As our analysis applies only for the domain  $R_G \leq r \leq R_{\max}$ , the most stringent constraint will be at the inner boundary of the shell,  $r = R_G$ . Applying this to the example of the solution with  $\tau = \frac{1}{2}$  and  $\kappa = \frac{1}{3}$ , which is associated with exactly flat rotation curves, one has from (13) that  $n(R_G) = \frac{M_G}{4\pi m R_G^3}$ , while  $\lambda = \frac{h}{mu} = \sqrt{\frac{2}{3}} \frac{h}{mv_\infty}$ . The condition (15) becomes

$$m^{8/3} \gg \frac{8\pi}{3^{5/3}} \left( \frac{\hbar \rho_G^{1/3}}{v_\infty} \right)^2, \quad (16)$$

where  $\rho_G$  is again the mean mass density inside the sphere of radius  $R_G$ . For an order of magnitude estimate, let us take  $\rho_G \sim 10^9 M_\odot/\text{kpc}^3$  along with  $v_\infty \sim 200$  km/s. Substituting into the right hand side of (16) gives  $\sim (100 \text{ eV})^{8/3}$ . Thus the classical approximation is valid provided that particle mass is significantly greater than  $\sim 100$  eV. In other words, corrections due to quantum statistics can only be significant in the spherical shell,  $R_G \leq r \leq R_{\max}$ , if the dark matter particle mass is  $\sim 100$  eV or less (smaller bounds result from typical densities of dwarf galaxies). However, since such hot dark matter scenarios are currently disfavored, classical statistics is all that is needed for this model.

## 4 Boltzmann fits

In section 2 we fit the rotation velocity data for galactic haloes to an eight-parameter series and found significant regions  $R_G \leq r \leq R_{\max}$  in the haloes where  $\rho(\phi)$  decreases exponentially. Here we directly compare the data in this region to the model of the self-gravitating isothermal Boltzmann gas constructed in the previous section. More specifically, we fit the rotational velocity data from THINGS[14] to solutions of (4) and (5). As stated in the introduction, our procedure is very different from the common practice of fitting the data using some particular density profile for the dark matter, such as NFW. The latter requires detailed knowledge of all the baryonic contributions, which are deduced from mass models. The results of such fits are highly dependent on the choice of mass models. On the other hand, precise density profiles for the baryonic contributions are not required in the analysis we do here. The baryonic component, nevertheless, plays an important role in our approach. It, along with the dark matter contribution to the mass  $M(R_G)$  in the interior region  $r \leq R_G$ , determine the second boundary condition in (4) at  $R_G$ , which gives the strength of the external gravitational field in the spherical shell  $R_G \leq r \leq R_{\max}$ . (In practice, we do the inverse. We determine the boundary condition from the fits, i.e., we obtain  $M(R_G)$  from the data.) As the purpose of this section is to test the validity of the model, it makes sense to restrict the fit to the region  $R_G \leq r \leq R_{\max}$  where the Boltzmann-like behavior was previously found.

The Boltzmann fits allow us to determine the three dimensionfull parameters of the model, namely,  $m/T$ ,  $\rho(R_G)$  and  $M(R_G)$ , for the given  $R_G$ . From them,

a) We compare the results for  $m/T$  to those found in section 2.

b) Using the Boltzmann form for the density (3), we numerically estimate the mass  $M_{(R_G, R_{\max})}$  of the region,  $R_G \leq r \leq R_{\max}$ . The mass of the Boltzmann-like region is simply

$$M_{(R_G, R_{\max})} = 4\pi \rho(R_G) \int_{R_G}^{R_{\max}} dr r^2 e^{-m\phi(r)/k_B T} \quad (17)$$

In order to understand what fraction of the total mass of the galaxy it represents, we compare  $M_{(R_G, R_{\max})}$  to the mass  $M(R_G)$  in the interior region  $r < R_G$ , and to the total baryonic mass of the galaxy, as was determined previously from a mass model.[14]

c) Lastly, we obtain fitted values for the dimensionless parameters  $\kappa$  and  $\tau$  and compare the results to the flat solution  $(\tau, \kappa) = (\frac{1}{2}, \frac{1}{3})$ .

We again consider the eight galaxies in the order: unbarred, weakly barred, barred and dwarf galaxies.

#### 4.1 NGC 2841

In subsection 2.1 the exponential behavior for  $\rho(\phi)$  was found in the region  $7 \text{ kpc} \leq r \leq 22 \text{ kpc}$  of the NGC 2841 halo. Here we perform the fit in this region of the rotation velocity data to solutions of (4) and (5). It is shown in figure 29. The fit is done to the midpoints [corresponding to the dots] of the error bars. The values found for the three dimensionfull parameters of the Boltzmann gas are:  $m/T \approx 205 \text{ eV/Kel}$ ,  $\rho(R_G) \approx 4.6 \times 10^7 M_\odot/\text{kpc}^3$  and  $M(R_G) \approx 1.7 \times 10^{11} M_\odot$ . The result for  $m/T$  is close to the value of  $\sim 190 \text{ eV/Kel}$  obtained in section 2. The latter corresponds to the average of  $-\frac{d \log \rho}{d \phi}$  over the domain  $7 < r < 22 \text{ kpc}$  in figure 5. One can also compare the results for  $\rho(R_G)$  and  $M(R_G)$  with those of the eight-parameter fit in section 2. For  $\rho(7 \text{ kpc})$ , the latter gives  $\sim 4.4 \times 10^7 M_\odot/\text{kpc}^3$ , which is close to the result obtained from the Boltzmann fit. More generally, in figure 30 we plot the Boltzmann gas density for the fitted values of the parameters and compare it with the density in figure 3, which was obtained from the eight-parameter series fit. Agreement is quite close beyond 10 kpc. (The analogous comparisons for the other seven galaxies [not shown here] are reasonably similar, with one exception.) To calculate  $M(R_G)$  from the eight-parameter fit, one can use  $M(R_G) = v(R_G)^2 R_G / G$ . The result is  $M(7 \text{ kpc}) \sim 1.67 \times 10^{11} M_\odot$ . This value is also close to the results we get for the Boltzmann fit.

We next numerically estimate the mass of the Boltzmann-like region  $7 < r < 22 \text{ kpc}$  using (17). We get  $M_{(7 \text{ kpc}, 22 \text{ kpc})} \approx 2.9 \times 10^{11} M_\odot$ . It is significantly greater than the mass  $M(R_G)$  of the inner region,  $r < 7 \text{ kpc}$ . Furthermore, it is also significantly greater than the sum of the baryonic mass contributions for NGC 2841 which were obtained from a mass model. [14] Summing the disk, bulge and HI gas masses cited in subsection 2.1 gives  $\sim 1.43 \times 10^{11} M_\odot$  [which in this example is close to the estimate for the mass  $M(R_G)$  in the inner region]. From these values one gets that the region exhibiting Boltzmann-like behavior is more than twice as massive as the baryonic component of the galaxy, and it therefore must consist mainly of dark matter.

From (8) we compute the fitted values for the dimensionless parameters  $\tau$  and  $\kappa$ . We get  $\tau \approx .37$  and  $\kappa \approx .42$ . This in contrast to the trivial isothermal solution  $(\tau, \kappa) = (\frac{1}{2}, \frac{1}{3})$ , associated with an exactly flat rotation curve. Since  $v(r)$  is far from being flat, it is a nontrivial result that the region  $7 < r < 22 \text{ kpc}$  is well described by a Boltzmann gas.

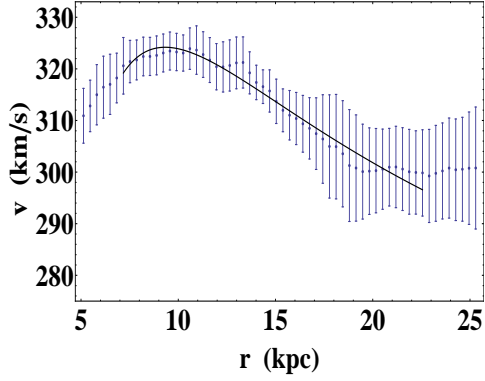


Figure 29: Fit of the rotation velocity data for NGC 2841 to a Boltzmann gas in the region  $7 \text{ kpc} \leq r \leq 22 \text{ kpc}$ . The fitted value for the three dimensionfull parameters of the Boltzmann gas are:  $m/T \approx 205 \text{ eV/Kel}$ ,  $\rho(R_G) \approx 4.6 \times 10^7 M_\odot/\text{kpc}^3$  and  $M(R_G) \approx 1.7 \times 10^{11} M_\odot$ .

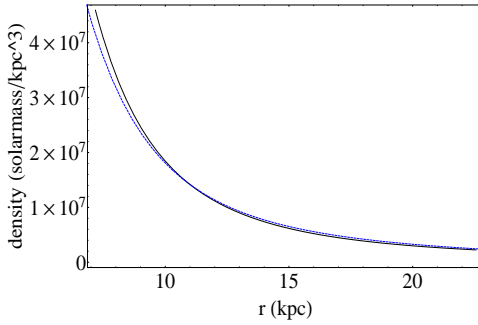


Figure 30: Plot of the Boltzmann gas density for the fitted values of the parameters (solid) compared to the density resulting from the eight-parameter series fit in section 2 which was obtained from the eight-parameter series fit restricted to the region  $7 \text{ kpc} \leq r \leq 22 \text{ kpc}$  (dashed).



## 4.2 NGC 5055

In subsection 2.2 the exponential behavior for  $\rho(\phi)$  was found in the region  $10 < r < 25$  kpc of the NGC 5055 halo. A fit in this region of the rotation velocity data to the solutions of (4) and (5) is shown in figure 31. The fitted value for the three dimensionfull parameters of the Boltzmann fit are:  $m/T \approx 300$  eV/Kel,  $\rho(R_G) \approx 5.7 \times 10^6 M_\odot/\text{kpc}^3$  and  $M(R_G) \approx 1.05 \times 10^{11} M_\odot$ . The fit for  $m/T$  is a bit below the average value of  $\sim 440$  eV/Kel found for this region from figure 8, but is somewhat sensitive to the choice of end points. Using (17), we can numerically estimate the mass of the region  $10 < r < 25$  kpc exhibiting Boltzmann-like behavior. We get  $M_{(10 \text{ kpc}, 25 \text{ kpc})} \approx 1.29 \times 10^{11} M_\odot$ . This is approximately the same as the estimated value of the mass  $M(R_G)$  in the interior region  $r < R_G$ , and also approximately the same as the sum of the baryonic mass contributions for NGC 5055 quoted in subsection 2.2. The latter is  $\sim 1.34 \times 10^{11} M_\odot$ . From (8) the fitted values for  $\tau$  and  $\kappa$  are  $\tau \approx 0.55$  and  $\kappa \approx 0.21$ , as compared with the flat solution  $(\tau, \kappa) = (\frac{1}{2}, \frac{1}{3})$ .

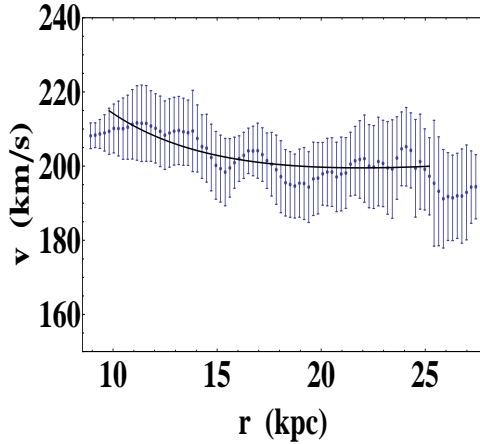


Figure 31: Fit of the rotation velocity data for NGC 5055 to a Boltzmann gas in the region  $10 \text{ kpc} \leq r \leq 25 \text{ kpc}$ . The fitted values for the three dimensionfull parameters of the Boltzmann gas are:  $m/T \approx 300$  eV/Kel,  $\rho(R_G) \approx 5.7 \times 10^6 M_\odot/\text{kpc}^3$  and  $M(R_G) \approx 1.05 \times 10^{11} M_\odot$ .

## 4.3 NGC 7331

In subsection 2.3 the exponential behavior for  $\rho(\phi)$  was found in the region  $8 < r < 16$  kpc of the NGC 7331 halo. A fit in this region of the rotation velocity data to the solutions of (4) and (5) is shown in figure 32. The fitted value for the three dimensionfull parameters of the Boltzmann fit are:  $m/T \approx 225$  eV/Kel,  $\rho(R_G) \approx 1.3 \times 10^7 M_\odot/\text{kpc}^3$  and  $M(R_G) \approx 1.3 \times 10^{11} M_\odot$ . The fit for  $m/T$  is to be compared with the average value of  $\sim 260$  eV/Kel found for this region from figure 10. Using (17), we can numerically estimate the mass of the region  $8 < r < 16$  kpc. We get  $M_{(8 \text{ kpc}, 16 \text{ kpc})} \approx .90 \times 10^{11} M_\odot$ , which is a little less than the mass  $M(R_G)$  in the interior region  $r < R_G$ . The sum of the quoted baryonic mass contributions for NGC 7331 in subsection 2.3, which were obtained from a mass model is  $\sim 1.925 \times 10^{11} M_\odot$ . [14] From (8) the fitted values for  $\tau$  and  $\kappa$  are  $\tau \approx 0.50$  and  $\kappa \approx 0.21$ .

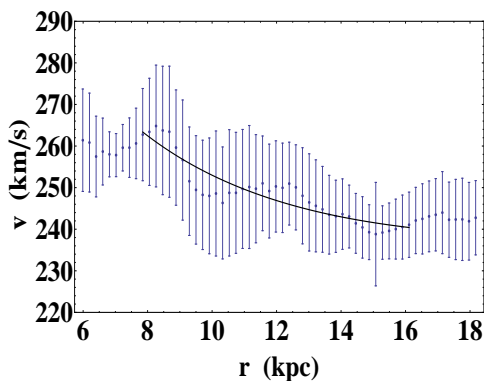


Figure 32: Fit of the rotation velocity data for NGC 7331 to a Boltzmann gas in the region  $8 \text{ kpc} \leq r \leq 16 \text{ kpc}$ . The fitted values for the three dimensionfull parameters of the Boltzmann gas are:  $m/T \approx 225 \text{ eV/Kel}$ ,  $\rho(R_G) \approx 1.3 \times 10^7 M_\odot/\text{kpc}^3$  and  $M(R_G) \approx 1.3 \times 10^{11} M_\odot$ .

#### 4.4 NGC 2403

In subsection 2.4 we found exponential behavior for  $\rho(\phi)$  in the region  $3 < r < 10 \text{ kpc}$  of the halo for weakly barred spiral galaxy NGC 2403. A fit of the rotation velocity data to the solutions of (4) and (5) in the region is shown in figure 33. The fitted value for the three dimensionfull parameters of the Boltzmann fit are:  $m/T \approx 1140 \text{ eV/Kel}$ ,  $\rho(R_G) \approx 3.5 \times 10^7 M_\odot/\text{kpc}^3$  and  $M(R_G) \approx 5.9 \times 10^9 M_\odot$ . The fit for  $m/T$  is close to the average value of  $\sim 1100 \text{ eV/Kel}$ , found for this region from figure 13. Using (17), we can numerically estimate the mass of the region  $3 < r < 10 \text{ kpc}$ . We get  $M_{(3 \text{ kpc}, 10 \text{ kpc})} \approx 3.25 \times 10^{10} M_\odot$ , which is over five times the mass  $M(R_G)$  in the interior region  $r < R_G$ . It is also much greater than the combined baryonic mass contributions from a mass model for NGC 2403, as was cited in subsection 2.4. The latter is  $\sim 7.7 \times 10^9 M_\odot$ . From (8) the fitted values for  $\tau$  and  $\kappa$  are  $\tau \approx 0.81$  and  $\kappa \approx 0.67$ .

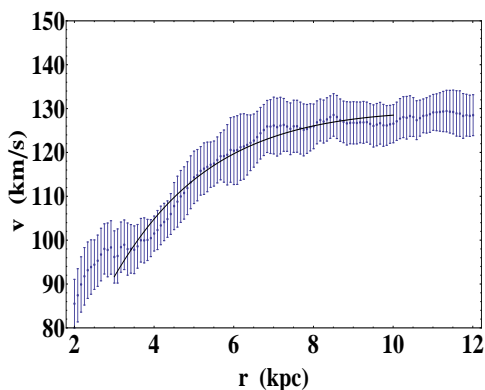


Figure 33: Fit of the rotation velocity data for NGC 2403 to a Boltzmann gas in the region  $3 \text{ kpc} \leq r \leq 10 \text{ kpc}$ . The fitted values for the three dimensionfull parameters of the Boltzmann gas are:  $m/T \approx 1140 \text{ eV/Kel}$ ,  $\rho(R_G) \approx 3.5 \times 10^7 M_\odot/\text{kpc}^3$  and  $M(R_G) \approx 5.9 \times 10^9 M_\odot$ .

## 4.5 NGC 2903

A fit of the rotation velocity data to the solutions of (4) and (5) in the region  $3 < r < 9$  kpc is shown in figure 34. The fitted value for the three dimensionfull parameters of the Boltzmann fit are:  $m/T \approx 580$  eV/Kel,  $\rho(R_G) \approx 1.6 \times 10^8 M_\odot/\text{kpc}^3$  and  $M(R_G) \approx 2.4 \times 10^{10} M_\odot$ . The result for  $m/T$  is compared with average value of  $\sim 490$  eV/Kel found in figure 16. Using (17), we can numerically estimate the mass of the region  $3 < r < 9$  kpc. We get  $M_{(3 \text{ kpc}, 9 \text{ kpc})} \approx 6.3 \times 10^{10} M_\odot$ . This is significantly greater than the mass  $M(R_G)$  in the interior region  $r < R_G$ , and also the combined baryonic mass contributions from a mass model for NGC 2903. Using the values quoted in subsection 2.5, the latter is  $\sim 2.06 \times 10^{10} M_\odot$ . From (8) the fitted values for  $\tau$  and  $\kappa$  are  $\tau \approx 0.41$  and  $\kappa \approx 0.90$ .

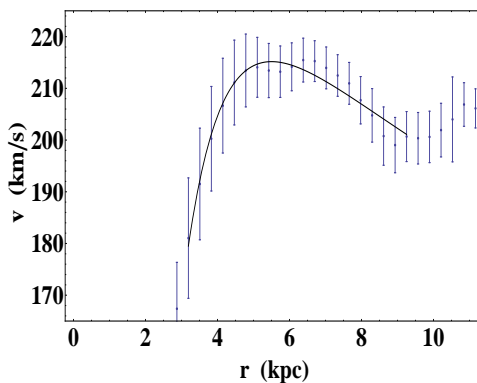


Figure 34: Fit of the rotation velocity data for NGC 2903 to a Boltzmann gas in the region  $3 \text{ kpc} \leq r \leq 9 \text{ kpc}$ . The fitted values for the three dimensionfull parameters of the Boltzmann gas are:  $m/T \approx 580$  eV/Kel,  $\rho(R_G) \approx 1.6 \times 10^8 M_\odot/\text{kpc}^3$  and  $M(R_G) \approx 2.4 \times 10^{10} M_\odot$ .

## 4.6 NGC 3521

A fit of the rotation velocity data to the solutions of (4) and (5) in the region  $7 < r < 15$  kpc is shown in figure 35. The fitted value for the three dimensionfull parameters of the Boltzmann fit are:  $m/T \approx 370$  eV/Kel,  $\rho(R_G) \approx 2.1 \times 10^7 M_\odot/\text{kpc}^3$  and  $M(R_G) \approx 8.9 \times 10^{10} M_\odot$ . The fit for  $m/T$  is close to the average value of 380 eV/Kel, found for this region in figure 19. Using (17), we can numerically estimate the mass of the region  $7 < r < 15$  kpc. We get  $M_{(7 \text{ kpc}, 15 \text{ kpc})} \approx 8.8 \times 10^{10} M_\odot$ , which is approximately the same as the mass  $M(R_G)$  in the interior region  $r < R_G$ . This is compared with the sum of the quoted baryonic mass contributions in subsection 2.6 for NGC 3521 of  $\sim 1.31 \times 10^{11} M_\odot$ . From (8) the fitted values for  $\tau$  and  $\kappa$  are  $\tau \approx 0.39$  and  $\kappa \approx 0.36$ .

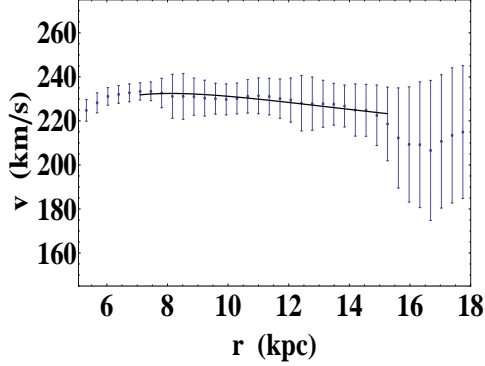


Figure 35: Fit of the rotation velocity data for NGC 3521 to a Boltzmann gas in the region  $7 \text{ kpc} \leq r \leq 15 \text{ kpc}$ . The fitted values for the three dimensionfull parameters of the Boltzmann gas are:  $m/T \approx 370 \text{ eV/Kel}$ ,  $\rho(R_{\text{G}}) \approx 2.1 \times 10^7 M_{\odot}/\text{kpc}^3$  and  $M(R_{\text{G}}) \approx 8.9 \times 10^{10} M_{\odot}$ .

#### 4.7 NGC 3198

For the case of the barred spiral galaxy NGC 3198, a fit of the rotation velocity data to the solutions of (4) and (5) in the region  $5 < r < 20 \text{ kpc}$  is shown in figure 36. The fitted value for the three dimensionfull parameters of the Boltzmann fit are:  $m/T \approx 800 \text{ eV/Kel}$ ,  $\rho(R_{\text{G}}) \approx 2.2 \times 10^7 M_{\odot}/\text{kpc}^3$  and  $M(R_{\text{G}}) \approx 1.9 \times 10^{10} M_{\odot}$ . The fit for  $m/T$  is within the range of values for this region found from figure 23. Using (17), we can numerically estimate the mass of the region  $5 < r < 20 \text{ kpc}$ . We get  $M_{(5 \text{ kpc}, 20 \text{ kpc})} \approx 8.9 \times 10^{10} M_{\odot}$ , which is much greater than the mass  $M(R_{\text{G}})$  in the interior region  $r < R_{\text{G}}$ . It is also greater than the sum of the stated baryonic masses for NGC 3198 in subsection 2.7. The latter is  $4.12 \times 10^{10} M_{\odot}$ . From (8) the fitted values for  $\tau$  and  $\kappa$  are  $\tau \approx 0.58$  and  $\kappa \approx 0.59$ .

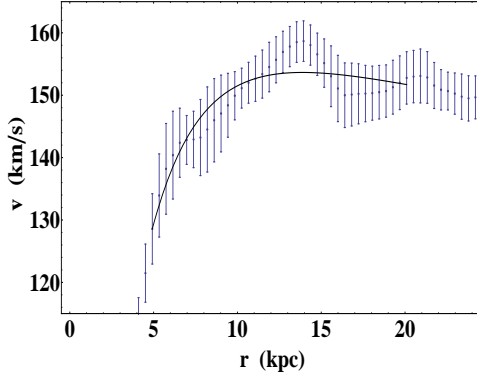


Figure 36: Fit of the rotation velocity data for NGC 3198 to a Boltzmann gas in the region  $5 \text{ kpc} \leq r \leq 20 \text{ kpc}$ . The fitted values for the three dimensionfull parameters of the Boltzmann gas are:  $m/T \approx 800 \text{ eV/Kel}$ ,  $\rho(R_{\text{G}}) \approx 2.2 \times 10^7 M_{\odot}/\text{kpc}^3$  and  $M(R_{\text{G}}) \approx 1.9 \times 10^{10} M_{\odot}$ .

## 4.8 DD0 154

Lastly, for the case of the dwarf galaxy DD0 154, a fit of the rotation velocity data to the solutions of (4) and (5) in the region  $1.5 < r < 6.5$  kpc is shown in figure 37. The fitted value for the three dimensionfull parameters of the Boltzmann fit are:  $m/T \approx 7500$  eV/Kel,  $\rho(R_G) \approx 1.2 \times 10^7 M_\odot/\text{kpc}^3$  and  $M(R_G) \approx 3.4 \times 10^8 M_\odot$ . The fit for  $m/T$  is within the range found for this region from figure 26. Using (17), we can numerically estimate the mass of the region  $1.5 < r < 6.5$  kpc. We get  $M_{(1.5 \text{ kpc}, 6.5 \text{ kpc})} \approx 3.2 \times 10^9 M_\odot$ , which is an order of magnitude bigger than the mass  $M(R_G)$  in the interior region  $r < R_G$ . It is also approximately an order of magnitude bigger than the sum of the stated baryonic masses for DD0 154 in subsection 2.8 ( $\sim 3.84 \times 10^8 M_\odot$ ). This is not surprising since the dark matter component is dominant in dwarf galaxies. From (8) the fitted values for  $\tau$  and  $\kappa$  are  $\tau \approx 1.13$  and  $\kappa \approx 0.62$ .

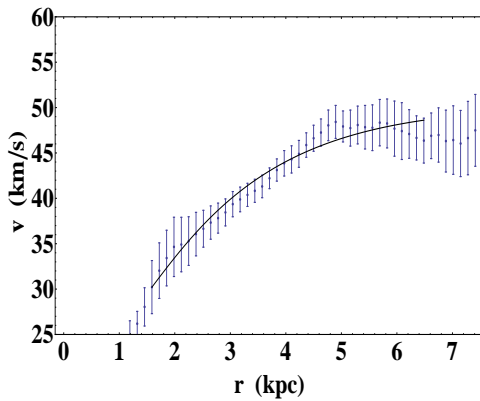


Figure 37: Fit of the rotation velocity data for DD0 154 to a Boltzmann gas in the region  $1.5 \text{ kpc} \leq r \leq 6.5 \text{ kpc}$ . The fitted values for the three dimensionfull parameters of the Boltzmann gas are:  $m/T \approx 7500$  eV/Kel,  $\rho(R_G) \approx 1.2 \times 10^7 M_\odot/\text{kpc}^3$  and  $M(R_G) \approx 3.4 \times 10^8 M_\odot$ .

## 5 Summary and Concluding Remarks

In section two we examined the rotation curve data of eight galaxies from THINGS[14], and searched for universal behavior for the function  $\rho(\phi)$ . We found indications that it has an exponential behavior in regions  $R_G \leq r \leq R_{\text{max}}$  of the haloes. We modeled the regions with an effective theory in section three. The dynamics in the spherical shell  $R_G \leq r \leq R_{\text{max}}$  was described by a self-gravitating isothermal gas, subject to an external gravitational field due to the inner-most region  $r \leq R_G$ . General solutions are specified by two dimensionless parameters, which were denoted by  $\tau$  and  $\kappa$ , while three dimensionfull parameters are required for a fit to the data. From typical rotation velocities, we checked that the (dark matter) particles responsible for flat rotation curves move nonrelativistically, and that quantum statistics is negligible in typical regions where the model has application. In section four, the rotation curve data was fit to solutions to the model in the regions  $R_G \leq r \leq R_{\text{max}}$  where Boltzmann-like behavior was found. The fits rely on the gravitational attraction to the baryonic matter in the inner region  $r \leq R_G$ , but do not require any detailed knowledge of the various density profiles; i.e., they do not require the use of mass models.

Our results for the fits and searches for Boltzmann-like behavior of the eight galaxies are summarized in tables 1 and 2 below. Table 1 contains two different estimates for  $m/T$  for each spherical shell region (columns four and five), along with distance scales for the various galaxies. The second column of table 1 lists the distances to the galaxies used in this article, while the third column contains the distance scale of the disks.[16] In column four we give the result for the mean values of  $-\frac{d\log\rho}{d\phi}$  in the regions (indicated below in parenthesis) where  $\rho(\phi)$  exhibited exponential behavior. (Recall,  $-\frac{d\log\rho}{d\phi}$  is a constant, namely  $m/T$ , for the Boltzmann gas.) The results were obtained using the eight-parameter series fits of the rotation velocity data described in section 2. The table shows that the regions exhibiting Boltzmann-like behavior are generally much larger than the disk scale. For the examples of NGC 5055, as well as for NGC 2841, these regions are  $\sim 15$  kpc, corresponding to roughly four times the distance scale of the disk. Also, the inner boundary  $r = R_G$  of the spherical shell is greater than the disk scale. Baryonic matter is expected to be subdominant at such distances. *Thus, dark matter should give the dominant contribution to the total mass density in the spherical shell  $R_G \leq r \leq R_{\max}$ , and it should therefore be responsible for the apparent Boltzmann-like behavior.*

As stated above, column four is an estimate of  $m/T$  in the region  $R_G \leq r \leq R_{\max}$ , which was obtained utilizing the eight-parameter fit. Column five of table 1 gives another determination for  $m/T$  in the same region. These values were obtained in section 4 by making a fit of the rotation curve data to solutions of the equation for a self-gravitating Boltzmann gas. The two different determinations of  $m/T$  are generally in agreement with each other for the eight galaxies. We note that after assuming that the (dark matter) mass  $m$  is a universal constant, we can compare the relative effective temperatures of (dark matter in) the spherical shells of the eight dark matter haloes. We get

$$T_{\text{NGC}2841} > T_{\text{NGC}7331} > T_{\text{NGC}3521} \sim T_{\text{NGC}5055} > T_{\text{NGC}2903} > T_{\text{NGC}3198} > T_{\text{NGC}2403} > T_{\text{DD0}154}$$

Table 2 reports on the mass estimates for the spherical shell  $R_G \leq r \leq R_{\max}$  and the inner region  $r \leq R_G$ . Table 2 also gives results for the dimensionless parameters  $(\tau, \kappa)$  for the Boltzmann fits. Column two lists the sum  $M_{\text{baryons}}$  of all the baryonic contributions to the mass of the galaxy reported in the literature. The disk and bulge contributions were obtained from a mass model in [14] (specifically, the model with fixed values of the mass to luminosity ratio and the diet Salpeter stellar initial mass function), while the HI gas mass estimates come from [17]. Column three gives the result for the mass  $M(R_G)$  in the interior region  $r \leq R_G$  obtained from the Boltzmann fits, while column four lists estimates of the total matter content in the spherical shell  $R_G \leq r \leq R_{\max}$  using (17). The table shows that for the majority of the galaxies, the regions exhibiting Boltzmann-like behavior are at least as massive, if not more, than the reported values for the sum of all the baryonic components of the galaxies. This is another indication that the region is strongly dominated by dark matter. Also, the spherical shells are, in general, more massive than the interior regions  $r \leq R_G$ . Two exceptional cases are NGC 7331 and NGC 3521, where the mass for the spherical shell  $M_{(R_G, R_{\max})}$  is less than  $M_{\text{baryons}}$ . On the other hand, for the case of the dwarf galaxy DD0 154, the region associated with the exponential behavior for  $\rho(\phi)$  is almost ten times as massive as the baryonic component of the galaxy.

Finally, column five of table 2 gives the fitted values for the dimensionless parameters  $\tau$  and  $\kappa$  defining the Boltzmann gas. The results vary from one galaxy to another, and generally differ from the special case of  $(\tau, \kappa) = (\frac{1}{2}, \frac{1}{3})$ , which corresponds to an exactly flat rotation curve. As was discussed in the introduction, isothermal behavior is obvious for the ideal case of exactly flat rotation curves. On the other hand, since from column five, the results are, in general, not in agreement with the exactly flat solution, the apparent isothermal behavior could not have been guessed from the outset.

Galaxy	distance [Mpc]	$R_{\text{disk}}$ [ kpc]	$-\left\langle \frac{d \log \rho}{d \phi} \right\rangle$ [ eV/Kel]	$m/T$ (Boltzmann fit) [ eV/Kel]
NGC 2841	14.1	3.5	190 ( $7 \leq r \leq 22$ kpc)	205 ( $7 \leq r \leq 22$ kpc)
NGC 5055	9.2	3.622	440 ( $10 \leq r \leq 25$ kpc)	300 ( $10 \leq r \leq 25$ kpc)
NGC 7331	14.2	3.2	260 ( $8 \leq r \leq 16$ kpc)	225 ( $8 \leq r \leq 16$ kpc)
NGC 2403	4.3	2.7	1100 ( $3 \leq r \leq 10$ kpc)	1140 ( $3 \leq r \leq 10$ kpc)
NGC 2903	9.4	3.0	490 ( $3 \leq r \leq 9$ kpc)	580 ( $3 \leq r \leq 9$ kpc)
NGC 3521	12.2	3.3	380 ( $7 \leq r \leq 15$ kpc)	370 ( $7 \leq r \leq 15$ kpc)
NGC 3198	14.1	4.0	820 ( $5 \leq r \leq 25$ kpc)	800 ( $5 \leq r \leq 20$ kpc)
DD0 154	4.2	.8	8600 ( $1.5 \leq r \leq 6.5$ kpc)	7500 ( $1.5 \leq r \leq 6.5$ kpc)

Table 1: Summary of estimates for  $m/T$  in the haloes of eight galaxies. The second column lists the distances to the galaxies used in this article. The third column quotes the distance scale of the disks from [16]. In column 4 we give the mean values of  $-\frac{d \log \rho}{d \phi}$  in regions (indicated below in parenthesis) where the derivatives are approximately constant. The values for  $m/T$  obtained from the fits of to the Boltzmann gas (for the region in the parenthesis below) is given in column 5.

We mention a few words about some of the galaxies in THINGS that were not analyzed here. Two galaxies, NGC 2976 and NGC 3627, were not considered at all because they contained too few data points for an eight-parameter fit. NGC 3031 and NGC 4736 may not be ideal candidates because they are reported as having non-circular motions. Also, at sufficient distances from the origin, the former is affected by tidal interactions from other members of the group (the M81 group, for the case of NGC 3031).[14] There are other galaxies in the survey with features that may not make them ideal candidates for an analysis of this sort as well, such as NGC 3627, which has a pronounced bar and an asymmetric spiral structure. The data for the remaining five galaxies in the survey did not exhibit any signs of universal behavior after doing the eight-parameter fit used in section 2. More specifically, we did not find convincing evidence of Boltzmann-like regions from the data for those galaxies.

In summary, from the rotation velocity data for 19 galaxies from THINGS, we found evidence of Boltzmann-like behavior in the haloes of eight galaxies, corresponding to approximately 40% of the sample. More specifically, after making the usual assumptions of spherical symmetry and that the rotation curves are generated by circular orbits, we showed that there were substantial regions of the haloes where the density decreased exponentially with the gravitational potential. For NGC 2841 and NGC 5055, agreement with Boltzmann-like behavior was found over a distance which was roughly four times the distance scale of the disk, and the relevant regions were estimated to be much more massive than the total baryonic masses of the galaxies. For the case of the dwarf galaxy DD0 154, the region exhibiting exponential behavior for  $\rho(\phi)$  was approximately six times larger than the disk scale and eight times more massive than the baryonic component, indicating that dark matter dominates the

Galaxy	$M_{\text{baryons}}$ [ $10^{10} M_{\odot}$ ]	$M(R_G)$ [ $10^{10} M_{\odot}$ ]	$M_{(R_G, R_{\text{max}})}$ [ $10^{10} M_{\odot}$ ]	$(\tau, \kappa)$
NGC 2841	14.3	17 ( $r \leq 7$ kpc)	29 ( $7 \leq r \leq 22$ kpc)	(.37, .42)
NGC 5055	13.4	10.5 ( $r \leq 10$ kpc)	12.9 ( $10 \leq r \leq 25$ kpc)	(.55, .21)
NGC 7331	19.25	13 ( $r \leq 8$ kpc)	9 ( $8 \leq r \leq 16$ kpc)	(.50, .21)
NGC 2403	.77	.59 ( $r \leq 3$ kpc)	3.25 ( $3 \leq r \leq 10$ kpc)	(.81, .67)
NGC 2903	2.06	2.4 ( $r \leq 3$ kpc)	6.3 ( $3 \leq r \leq 9$ kpc)	(.41, .90)
NGC 3521	13.1	8.9 ( $r \leq 7$ kpc)	8.8 ( $7 \leq r \leq 15$ kpc)	(.39, .36)
NGC 3198	4.12	1.9 ( $r \leq 5$ kpc)	8.9 ( $5 \leq r \leq 20$ kpc)	(.58, .59)
DD0 154	.0384	.034 ( $r \leq 1.5$ kpc)	.32 ( $1.5 \leq r \leq 6.5$ kpc)	(1.13, .62)

Table 2: Summary of mass estimates and  $(\tau, \kappa)$  for eight galaxies. Column 2 lists the total mass baryonic mass of the galaxy, as determined from a mass model. [14] In column 3, we give the value of the mass  $M(R_G)$  in the interior region ( $r \leq R_G$ ), obtained from the fit to the Boltzmann gas. The mass  $M_{(R_G, R_{\text{max}})}$  of the Boltzmann-like region, estimated using (17), appears in column 4. Column 5 lists the fitted values of the dimensionless parameters  $\tau$  and  $\kappa$ .

region. In all cases, the exponential behavior breaks down at short and large distances. The breakdown at extremely large distances may indicate that the dynamics described by (5) is not valid when densities go below a certain threshold. It is not hard to understand the breakdown at short distances, since the assumptions of symmetry and a single-component gas are not valid approximations close to the disk.

A number of improvements can be performed to the model presented in section 3 and its fits of galactic haloes in sections 4. The most obvious are to drop the assumption of spherical symmetry, and to take into account effects of the HI gas present in the haloes. Furthermore, one can try to extend the analysis to include the interior region. As densities grow in the interior, it may then be of interest to consider the effect of quantum statistics.

Finally, the fact that we have evidence of some Boltzmann-like behavior in substantial regions of eight galactic haloes may not be accidental, as it may signal the presence of (non gravitational) dark matter self-interactions. Moreover, it is an indication that such interactions could be sufficient in strength and number for the system to settle down to an equilibrium configuration.

## Acknowledgments

We are very grateful to P. Biermann, R. Buta, N. Okada and J. Reichenbacher for valuable discussions. We are also grateful to Erwin de Blok for providing us with rotation curve data from THINGS. A.S. was supported in part by the DOE, Grant No. DE-FG02-10ER41714.



## REFERENCES

- [1] J. F. Navarro, C. S. Frenk and S. D. M. White, “A Universal density profile from hierarchical clustering,” *Astrophys. J.* **490**, 493 (1997).
- [2] S. -H. Oh, W. J. G. de Blok, E. Brinks, F. Walter and R. C. Kennicutt, Jr, “Dark and luminous matter in THINGS dwarf galaxies,” arXiv:1011.0899 [astro-ph.CO].
- [3] N. Frusciante, P. Salucci, D. Vernieri, J. M. Cannon and E. C. Elson, “The Distribution of Mass in the Orion Dwarf Galaxy,” arXiv:1206.0314 [astro-ph.CO].
- [4] D. N. Spergel and P. J. Steinhardt, “Observational evidence for selfinteracting cold dark matter,” *Phys. Rev. Lett.* **84**, 3760 (2000); R. Dave, D. N. Spergel, P. J. Steinhardt and B. D. Wandelt, “Halo properties in cosmological simulations of selfinteracting cold dark matter,” *Astrophys. J.* **547**, 574 (2001).
- [5] R. N. Mohapatra, S. Nussinov and V. L. Teplitz, “Mirror matter as selfinteracting dark matter,” *Phys. Rev. D* **66**, 063002 (2002).
- [6] R. Foot and R. R. Volkas, “Spheroidal galactic halos and mirror dark matter,” *Phys. Rev. D* **70**, 123508 (2004).
- [7] L. Ackerman, M. R. Buckley, S. M. Carroll and M. Kamionkowski, “Dark Matter and Dark Radiation,” *Phys. Rev. D* **79**, 023519 (2009).
- [8] M. R. Buckley and P. J. Fox, “Dark Matter Self-Interactions and Light Force Carriers,” *Phys. Rev. D* **81**, 083522 (2010).
- [9] J. L. Feng, M. Kaplinghat and H. -B. Yu, “Halo Shape and Relic Density Exclusions of Sommerfeld-Enhanced Dark Matter Explanations of Cosmic Ray Excesses,” *Phys. Rev. Lett.* **104**, 151301 (2010).
- [10] S. Chang, A. Pierce and N. Weiner, “Momentum Dependent Dark Matter Scattering,” *JCAP* **1001**, 006 (2010).
- [11] A. Loeb and N. Weiner, “Cores in Dwarf Galaxies from Dark Matter with a Yukawa Potential,” *Phys. Rev. Lett.* **106**, 171302 (2011).
- [12] T. Lin, H. -B. Yu and K. M. Zurek, “On Symmetric and Asymmetric Light Dark Matter,” *Phys. Rev. D* **85**, 063503 (2012); S. Tulin, H. -B. Yu and K. M. Zurek, “Resonant Dark Forces and Small Scale Structure,” *Phys. Rev. Lett.* **110**, no. 11, 111301 (2013); “Beyond Collisionless Dark Matter: Particle Physics Dynamics for Dark Matter Halo Structure,” arXiv:1302.3898 [hep-ph]; M. Kaplinghat, S. Tulin and H. -B. Yu, “Self-interacting Dark Matter Benchmarks,” arXiv:1308.0618 [hep-ph].
- [13] C. Destri, H. J. de Vega and N. G. Sanchez, “Fermionic warm dark matter produces galaxy cores in the observed scales,” arXiv:1204.3090 [astro-ph.CO].
- [14] W. J. G. de Blok, F. Walter, E. Brinks, C. Trachternach, S-H. Oh and R. C. Kennicutt, Jr., “High-Resolution Rotation Curves and Galaxy Mass Models from THINGS,” *Astron. J.* **136**, 2648 (2008).
- [15] Emden, R., ‘Gaskugeln: Anwendungen der Mechanischen Warmetheorie auf Kosmologische und Meteorologische Probleme’, Teubner, Berlin (1907).

- [16] P. D. Mannheim and J. G. O'Brien, "Fitting galactic rotation curves with conformal gravity and a global quadratic potential," *Phys. Rev. D* **85**, 124020 (2012).
- [17] F. Walter, E. Brinks, W. J. G. de Blok, F. Bigiel, R. C. Kennicutt, Jr., M. D. Thornley and A. K. Leroy, "THINGS: The HI Nearby Galaxy Survey," *Astron. J.* **136**, 2563 (2008).
- [18] P. J. E. Peebles, "Principles of physical cosmology," Princeton, USA: Univ. Pr. (1993) 718 p.
- [19] F. K. Liu, "Polytropic gas spheres: An Approximate analytic solution of the Lane-Emden equation," *Mon. Not. Roy. Astron. Soc.* **281**, 1197 (1996).
- [20] P. Natarajan and D. Lynden-Bell, "An analytic approximation to the isothermal sphere," *astro-ph/9604084*.
- [21] Y. Mishchenko and C. -R. Ji, "Molar mass estimate of dark matter from the dark mass distribution measurements," *Phys. Rev. D* **68**, 063503 (2003).
- [22] D. M. Christodoulou and D. Kazanas, "Exact Solutions of the Isothermal Lane-Emden Equation with Rotation and Implications for the Formation of Planets and Satellites," [arXiv:0706.3205 [astro-ph]].